

Article

# Modulating Interfacial Charge Transfer Behavior through the Construction of a Hetero-Interface for Efficient Photoelectrochemical Water Splitting

Li Xu <sup>1,†</sup>, Jingjing Quan <sup>1,†</sup>, Li Xu <sup>2,†</sup>, Meihua Li <sup>1</sup>, Chenglong Li <sup>1</sup>, Saqib Mujtaba <sup>1</sup> , Xingming Ning <sup>1,\*</sup>, Pei Chen <sup>1,\*</sup>, Qiang Weng <sup>1</sup>, Zhongwei An <sup>1</sup> and Xinbing Chen <sup>1,\*</sup>

<sup>1</sup> Key Laboratory of Applied Surface and Colloid Chemistry (MOE), Ministry of Education, Shaanxi Key Laboratory for Advanced Energy Devices, Shaanxi Engineering Laboratory for Advanced Energy Technology, International Joint Research Center of Shaanxi Province for Photoelectric Materials Science, School of Materials Science and Engineering, Shaanxi Normal University, Xi'an 710119, China; xuli00@snnu.edu.cn (L.X.); jjquan2022@163.com (J.Q.); meihuali@snnu.edu.cn (M.L.); 330796680@snnu.edu.cn (C.L.); smujtaba304@gmail.com (S.M.); wengqiang@snnu.edu.cn (Q.W.); gmecazw@163.com (Z.A.)

<sup>2</sup> School of Chemistry and Chemical Engineering, Hexi University, Zhangye 734000, China; xuli\_hxu@163.com

\* Correspondence: ningxingming@snnu.edu.cn (X.N.); chenpei@snnu.edu.cn (P.C.); chenxinbing@snnu.edu.cn (X.C.)

† These authors contributed equally to this work.

**Abstract:** Surface-coupled transition metal oxyhydroxide (TMOOH) on semiconductor (SC)-based photoanodes are effective strategies for improving photoelectrochemical (PEC) performance. However, there is a substantial difference between the current density and theoretical value due to the inevitable interfacial charge recombination of SC/TMOOH. Here, we employ BiVO<sub>4</sub>/FeNiOOH as a model, constructing the BiVO<sub>4</sub>/MnO<sub>x</sub>/CoO<sub>x</sub>/FeNiOOH integrated system by introducing a novel hetero-interface regulation unit, i.e., MnO<sub>x</sub>/CoO<sub>x</sub>. As expected, the optimized integrated system demonstrates a photocurrent density as high as 5.0 mA/cm<sup>2</sup> at 1.23 V versus the reversible hydrogen electrode (RHE) under 1 sun AM 1.5G illumination, accompanied by 12-h stability. The detailed electrochemical analysis and intensity modulated photocurrent spectroscopy (IMPS) have confirmed that the high PEC performance mainly originates from the hetero-interface structure, which not only suppresses the interfacial charge recombination by accelerating the photogenerated hole transfer kinetics from BiVO<sub>4</sub> to FeNiOOH but promotes the kinetics of surface oxygen evolution reaction (OER). Notably, these findings can also be extended to other structures (CeO<sub>x</sub>/CoO<sub>x</sub>), reflecting its universality. This finding has provided a new insight into the highly efficient solar energy conversion in the SC/TMOOH system.

**Keywords:** interface recombination; hetero-interface; interfacial charge transfer; kinetics; photoelectrochemical



**Citation:** Xu, L.; Quan, J.; Xu, L.; Li, M.; Li, C.; Mujtaba, S.; Ning, X.; Chen, P.; Weng, Q.; An, Z.; et al. Modulating Interfacial Charge Transfer Behavior through the Construction of a Hetero-Interface for Efficient Photoelectrochemical Water Splitting. *Separations* **2024**, *11*, 109. <https://doi.org/10.3390/separations11040109>

Academic Editor: Dimosthenis Giokas

Received: 22 February 2024

Revised: 26 March 2024

Accepted: 27 March 2024

Published: 1 April 2024



**Copyright:** © 2024 by the authors. Licensee MDPI, Basel, Switzerland. This article is an open access article distributed under the terms and conditions of the Creative Commons Attribution (CC BY) license (<https://creativecommons.org/licenses/by/4.0/>).

## 1. Introduction

Photoelectrochemical (PEC) water splitting is an effective strategy to achieve the goal of “double carbon” [1–4]. The overall PEC water-splitting process mainly includes light harvesting, photogenerated charge separation, and surface catalysis [5]. Among the above-mentioned processes, the slow surface reaction kinetics results in severe recombination of photogenerated charge carriers, greatly limiting the overall conversion efficiency from solar energy to hydrogen and seriously impeding the further development of this process [6,7].

Recently, a large number of researchers found that coating electrocatalyst on semiconductor (SC)-based photoanodes can effectively reduce the energy barrier of the surface catalytic reaction, accelerate the kinetics of OER, and thus enhance the PEC water splitting performance [8–12]. Among various electrocatalysts, transition metal hydroxide oxides (TMOOH) have gained significant attention due to their excellent stability, earth abundance,

and highly active sites [8,13]. For example, Bi et al. [12] upgraded the single-component TMOOH to binary TMOOH and found that the PEC performance was obviously improved. Kim et al. [8] reported that the resulting integrated system of BiVO<sub>4</sub>/FeOOH/NiOOH presented a photocurrent density of 2.73 mA/cm<sup>2</sup> at 0.6 V vs. RHE. Based on the above discussion, we can reveal that the coupling of electrocatalysts can effectively enhance the efficiency of PEC hydrogen evolution. However, there is still a significant gap between the photocurrent density of the current integrated system and the theoretical value [14–16].

Recently, interface engineering has been considered as one of the most desirable strategies to suppress interface charge recombination occurring at the SC/TMOOH interface [17,18]. Therein, introducing transition metal compounds, acting as an interface mediator, into the SC/TMOOH system is an efficient and common strategy for further increasing the photocurrent density. As reported earlier, Zhao et al. [19] noted that loading Co-Pi acts as a passivation layer, leading to a significant improvement in PEC performance. Later, Li's team [20] incorporated a storage layer, ferrihydrite (Fh), into the Ta<sub>3</sub>N<sub>5</sub> photoanode, and presented a noticeable increase in photocurrent density compared to the bare Ta<sub>3</sub>N<sub>5</sub> counterparts. In addition, the Sun group [17] proved that incorporation of single-atomic Ni-N<sub>4</sub>-O moiety in FeOOH/BiVO<sub>4</sub> can accelerate hole transfer kinetics and thus improve PEC water splitting activity, accompanied by long-term photostability.

Despite these interface engineering strategies having been verified for significantly improving PEC water splitting performance, the actual photocurrent density of SC/X/TMOOH (where X stands for interface mediator) is still lower than its theoretical value. Nevertheless, these previous works only pay more attention to either the SC/X or SC/electrolyte interfaces rather than engineering these interfaces to achieve a smart SC/X/TMOOH photoelectrode for further enhancing the efficiency of SC-based photoanode. Encouraged by the above findings, we have constructed a novel interface modulation unit (hetero-interface) aiming at accelerating charge transfer kinetics and achieving high-efficiency PEC performance. Here, BiVO<sub>4</sub> (named BV) served as the light capture material due to its narrow bandgap (ca. 2.4 eV), good stability, and appropriate band edge position [21–23]. Besides, a hetero-interface (MnO<sub>x</sub>/CoO<sub>x</sub>) with high chemical stability, excellent catalytic activity [24,25], and variable valence states is introduced. Of course, BV/FeNiOOH, as a “star” system, is used to prove a relevant positive effect on modulating interfacial charge transfer behavior during PEC water splitting.

Herein, we report a one-stone-two-birds strategy to engineer the SC/TMOOH/electrolyte interface for highly efficient PEC performance by introducing a hetero-interface (MnO<sub>x</sub>/CoO<sub>x</sub>) into the SC/TMOOH coupling system. As a result, the optimized BV/MnO<sub>x</sub>/CoO<sub>x</sub>/FeNiOOH integrated system shows an impressive photocurrent density of 5.0 mA/cm<sup>2</sup> at 1.23 V vs. RHE under AM 1.5G illumination and excellent stability. Electrochemical characterization and dynamics measurement confirm that both interface charge transfer occurring at BV/TMOOH and surface catalysis dynamics at TMOOH/electrolyte are enhanced through the introduction of MnO<sub>x</sub>/CoO<sub>x</sub>. More importantly, this smart strategy can also be applied to other similar hetero-interfaces (CeO<sub>x</sub>/CoO<sub>x</sub>), exhibiting its universality. These results provide a guiding design approach for improving solar energy conversion in SC/TMOOH systems.

## 2. Materials and Methods

### 2.1. Chemical Reagents

Potassium iodide (KI, ≥99.00%), potassium ferrocyanide (K<sub>4</sub>[Fe(CN)<sub>6</sub>], ≥99.00%), potassium ferricyanide (K<sub>3</sub>[Fe(CN)<sub>6</sub>], ≥99.50%), boric acid (H<sub>3</sub>BO<sub>3</sub>, 99.00%), iron sulfate heptahydrate (FeSO<sub>4</sub>·7H<sub>2</sub>O, ≥99.00%), dimethyl sulfoxide (DMSO, >99.00%), vanadyl acetylacetonate (VO(acac)<sub>2</sub>, 98.00%), manganese nitrate tetrahydrate (Mn(NO<sub>3</sub>)<sub>2</sub>·4H<sub>2</sub>O, 98.00%), and cobalt nitrate hexahydrate (Co(NO<sub>3</sub>)<sub>2</sub>·6H<sub>2</sub>O, 99.00%) were obtained from Aladdin Biochemical Technology Co., Ltd. (Shanghai, China). Bismuth nitrate pentahydrate (Bi(NO<sub>3</sub>)<sub>3</sub>·5H<sub>2</sub>O, 98.00%) was selected from Alfa Aesar (China) Chemicals Co., Ltd. Sodium sulfite (Na<sub>2</sub>SO<sub>3</sub>, ≥97.00%), Benzoquinone (C<sub>6</sub>H<sub>4</sub>O<sub>2</sub>, ≥98.00%), and nickel(II) nitrate hexahydrate (Ni(NO<sub>3</sub>)<sub>2</sub>·6H<sub>2</sub>O, ≥98.00%) were obtained from Sinopharm Chemical Reagent Co., Ltd. (Shanghai, China). Cerium(III) nitrate hydrate (Ce(NO<sub>3</sub>)<sub>3</sub>·xH<sub>2</sub>O, x = 6–7, 99.998%)

was obtained from Macklin Biochemical Co., Ltd. (Shanghai, China). Fluorine-doped SnO<sub>2</sub> (FTO, 14 Ω per square) substrates were purchased from Jinge Solar Energy Technology Co., Ltd. (Wuhan, China). Deionized water (18.25 MΩ cm) was obtained by a Milli-Q system.

## 2.2. Materials Preparation

### 2.2.1. Preparation of BiVO<sub>4</sub> (BV) Films

BV films were prepared by a two-step process according to the previously reported method [26]. Typically, 0.015 M Bi(NO<sub>3</sub>)<sub>3</sub>·5H<sub>2</sub>O was dissolved in 0.4 M KI (100 mL) and the pH value of the above solution was adjusted to 1.7 by using concentrated HNO<sub>3</sub> solution, which was named solution A. Subsequently, the solution B (p-benzoquinone, 4.6 mmol) was dissolved in 20 mL of ethanol, then, the above solution B and solution A were mixed and stirred for 20 min to achieve the precursor solution. The deposition process of BiOI films was carried out at −0.1 V vs. Ag/AgCl for 300 s. 0.2 M VO(acac)<sub>2</sub> (150 μL), dissolved in a DMSO, dropped onto a BiOI film, and annealed in air for 2 h (450 °C). The target photoanode was immersed in 0.5 M K<sub>3</sub>BO<sub>3</sub> solution (30 min) to remove excess V<sub>2</sub>O<sub>5</sub>. Finally, the BV photoanode was rinsed with second water and dried at room temperature.

### 2.2.2. Preparation of BV/MnO<sub>x</sub>/CoO<sub>x</sub> and BV/CeO<sub>x</sub>/CoO<sub>x</sub>

The BV/MnO<sub>x</sub>/CoO<sub>x</sub> and BV/CeO<sub>x</sub>/CoO<sub>x</sub> were obtained by electrodeposition and calcination methods. For BV/MnO<sub>x</sub>/CoO<sub>x</sub>, the electrolyte, containing 16 mM Mn(NO<sub>3</sub>)<sub>2</sub>·4H<sub>2</sub>O and 16 mM Co(NO<sub>3</sub>)<sub>2</sub>·6H<sub>2</sub>O, was prepared in deionized water for electrodeposition. The electrodeposition of Mn(OH)<sub>x</sub>/Co(OH)<sub>x</sub> on the BV surface was performed by a typical three-electrode cell using BV photoanode as the working electrode (WE), Ag/AgCl electrode acted as the reference electrode (RE), and platinum mesh as a counter electrode (CE). Electrodeposition was carried out at a constant potential of −0.4 V versus Ag/AgCl and the deposition time was 50 s at room temperature. Subsequently, the obtained BV/Mn(OH)<sub>x</sub>/Co(OH)<sub>x</sub> photoanodes (after rinsing with deionized water and drying) were heated at 300 °C for 2 h (2 °C/min) by a muffle furnace. Finally, the resulting BV/MnO<sub>x</sub>/CoO<sub>x</sub> photoanode was rinsed with deionized water before use. The same experimental conditions were carried out to prepare the BV/CeO<sub>x</sub>/CoO<sub>x</sub> photoanode.

### 2.2.3. Preparation of BV/MnO<sub>x</sub>/CoO<sub>x</sub>/FeNiOOH and BV/CeO<sub>x</sub>/CoO<sub>x</sub>/FeNiOOH Photoanodes

Photodeposition of FeNiOOH on the BV/MnO<sub>x</sub>/CoO<sub>x</sub> photoanode was performed in a mixed solution containing FeSO<sub>4</sub>·7H<sub>2</sub>O (25 mM) and Ni(NO<sub>3</sub>)<sub>2</sub>·6H<sub>2</sub>O (75 mM). Prior to the deposition of FeNiOOH, the obtained solution was purged with N<sub>2</sub> for half an hour. Similarly, a three-electrode cell was used, which was composed of a WE (BV/MnO<sub>x</sub>/CoO<sub>x</sub>), a CE (platinum mesh), and a RE (Ag/AgCl). A Xe arc lamp (300 W, Perfectlight Technology Co., Ltd. (Beijing, China), PLS-SXE300D) with an AM 1.5G filter was chosen as the light source and the light intensity at the photoanode surface was 100 mW/cm<sup>2</sup> (back-side illumination). During illumination, the photogenerated holes from BV were used to oxidize metal ions to a high valence state. To boost photodeposition, the deposition time is 600 s (0.3 V vs. Ag/AgCl). The same procedure was used to obtain BV/CeO<sub>x</sub>/CoO<sub>x</sub>/FeNiOOH photoanode except for the WE, which was a BV/CeO<sub>x</sub>/CoO<sub>x</sub> photoanode.

### 2.2.4. Preparation of BV/FeNiOOH Photoanodes

The same procedure was used to obtain a BV/FeNiOOH photoanode except for the WE, which was a BV photoanode.

## 2.3. Structural Characterization

The morphologies of photoelectrodes were probed by field emission scanning electron microscopy (FESEM, SU8020, Hitachi, Tokyo, Japan). The chemical states and chemical composition were determined by X-ray photoelectron spectroscopy (XPS, Escalab Xi<sup>+</sup>, Waltham, MA, USA). The crystal structures of different samples were obtained from powder

X-ray diffraction (XRD, SmartLab 9 KW, Rigaku, Tokyo, Japan) at room temperature. Raman spectroscopy was measured by a Microscopic confocal laser Raman spectrometer. The optical properties of different photoelectrodes were investigated by ultraviolet–visible (UV–vis) absorption spectroscopy (Shimadzu UV-3600, Shimadzu, Kyoto, Japan). The photoluminescence (PL) tests were carried out on a FL 8500 fluorescence spectrophotometer (PerkinElmer, Waltham, MA, USA) at room temperature and the excitation wavelength of 355 nm.

#### 2.4. Electrochemical Measurements

Electrochemical tests of different BV-based photoelectrodes were tested on an electrochemical workstation (CHI760E) through a traditional three-electrode system in 1.0 M  $K_3BO_3$  electrolyte. Cyclic voltammogram (CV) curves were obtained at a scan rate of 50 mV/s.

#### 2.5. Photoelectrochemical (PEC) Measurements

PEC activities of BV-based photoanodes were conducted on electrochemical workstation by a common three-electrode configuration in  $K_3BO_3$  (1 M) electrolyte (50 mV/s). In the work, BV based photoanodes were illuminated under AM 1.5G light (exposure area of 1 cm<sup>2</sup>). All the potentials versus Ag/AgCl were adjusted to the potentials versus RHE according to the Nernst equation:  $E_{(RHE)} = E_{(Ag/AgCl)} + 0.197 + 0.0591 \text{ pH}$ .

The following PEC properties were measured by Autolab M204 using a three-electrode system. Electrochemical impedance spectroscopy (EIS) was performed at an AC voltage amplitude of 10 mV under AM 1.5G illumination at the frequency range from 10 KHz to 0.1 Hz.

The intensity modulated photocurrent spectroscopy (IMPS) of different BV-based photoanodes were obtained through the photochem system (LED, 470 nm, 20% light intensity modulation) of Autolab M204 in the frequency range of 10 KHz to 0.1 Hz in 1 M  $K_3BO_3$ . And the  $I-t$  curves were measured at the same potential with IMPS (LED, 470 nm).

According to our previous work [23],  $\tau_d$  can be calculated by using the following formula:

$$\tau_d = \frac{1}{2\pi f_{IMPS}} \quad (1)$$

where  $f_{IMPS}$  refers to the frequency located at the lowest point of IMPS plot.

The applied bias photon-to-current efficiencies (ABPE) of different photoanodes were calculated by using the following equation [27]:

$$ABPE(\%) = \frac{(J_{light} - J_{dark}) \times (1.23 - V_{app})}{P_{light}} \times 100\% \quad (2)$$

where  $J_{light}$  and  $J_{dark}$  are the photocurrent density (mA/cm<sup>2</sup>) in the light and dark, respectively.  $V_{app}$  is the applied potential (vs. RHE) and  $P_{light}$  is the power intensity of AM 1.5G (100 mW/cm<sup>2</sup>).

The surface charge separation efficiencies ( $\eta_{sep}$ ) of BV/MnO<sub>x</sub>/CoO<sub>x</sub>/FeNiOOH and BV can be obtained using the following equation [17]:

$$\eta_{sep}(\%) = \frac{J_{H_2O}}{J_{Na_2SO_3}} \times 100\% \quad (3)$$

$J_{H_2O}$  and  $J_{Na_2SO_3}$  are the photocurrent density obtained in a  $K_3BO_3$  electrolyte (pH 9.5) without or with  $Na_2SO_3$ , respectively.

### 3. Results and Discussion

Figure 1a illustrates the preparation process of the BV/MnO<sub>x</sub>/CoO<sub>x</sub>/FeNiOOH integrated system. In the first step, a porous BV film is grown on a fluorine-doped tin oxide (FTO) glass substrate. Secondly, the interface mediator, namely, a MnO<sub>x</sub>/CoO<sub>x</sub> thin

layer, is coated on the BV surface. Finally, the FeNiOOH is deposited on the surface of BV/MnO<sub>x</sub>/CoO<sub>x</sub> to achieve a BV/MnO<sub>x</sub>/CoO<sub>x</sub>/FeNiOOH integrated system. For surface morphology, advanced characterization techniques like scanning electron microscopy (SEM) were used to explore its microstructure and nanoscale morphology. As described in Figure S1, BV is evenly dispersed on the FTO surface and displays its unique worm-like porous structure (average diameter of 100–300 nm). X-ray diffraction (XRD) was employed to investigate the crystal structure of relevant samples. As shown in Figure S2, the BV film belongs to a monoclinic structure (PDF#14-0688) [21,28–30], which is consistent with previous reports. In addition, X-ray photoelectron spectroscopy (XPS) measurement was performed to further investigate the chemical state. From Figure S3, we can observe the two evident peaks of Bi 4f at 158.8 eV (Bi 4f<sub>7/2</sub>) and 164.1 eV (Bi 4f<sub>5/2</sub>), corresponding to Bi<sup>3+</sup> in BV. Similarly, the peaks at 516.3 eV (V 2p<sub>3/2</sub>) and 523.8 eV (V 2p<sub>1/2</sub>) in high resolution V 2p XPS spectra could be indexed to the V<sup>3+</sup> in BV [31]. Moreover, these characteristic Raman peaks further suggest that the BV photoelectrode has been successfully obtained (Figure S4) [23], which is further supported by XPS survey spectra (Figure S3).

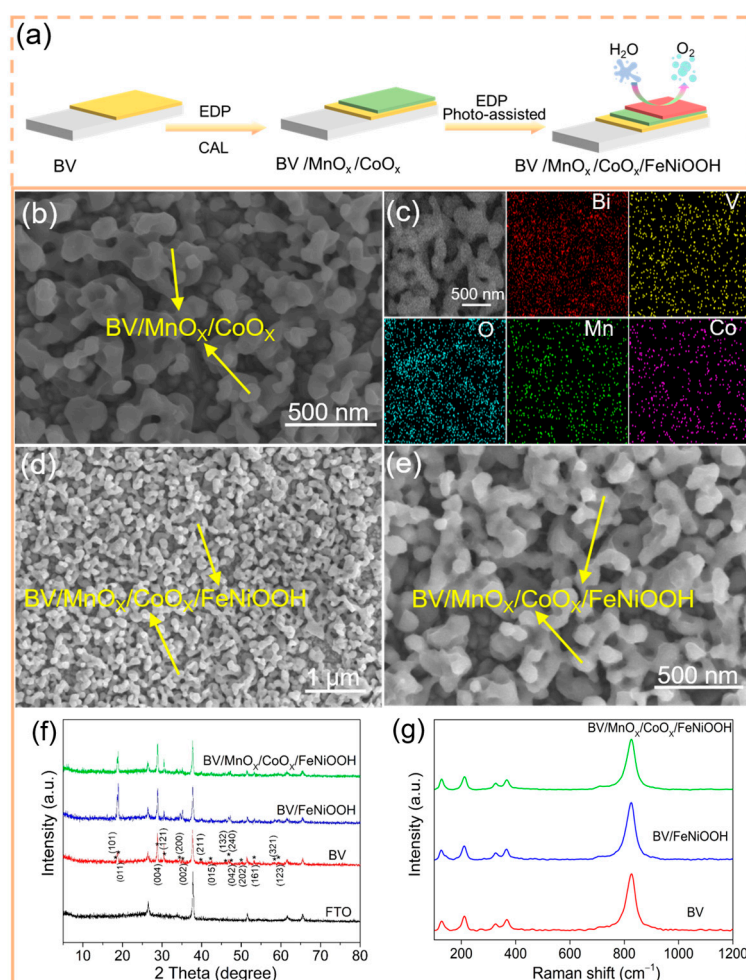


**Figure 1.** (a) Schematic illustration of the preparation procedure for BV/MnO<sub>x</sub>/CoO<sub>x</sub>/FeNiOOH; (b) SEM image of BV/MnO<sub>x</sub>/CoO<sub>x</sub>; (c) SEMEDS elemental mapping images of Bi, V, Mn, Co, and O. (d,e) SEM images of BV/MnO<sub>x</sub>/CoO<sub>x</sub>/FeNiOOH; (f) XRD patterns of different photoanodes; (g) Raman spectra.

Subsequently, an interface mediator, namely MnO<sub>x</sub>/CoO<sub>x</sub>, is loaded on the BV surface by electrodeposition and calcination methods. Interestingly, in comparison to pure BV, BV/MnO<sub>x</sub>/CoO<sub>x</sub> presents relatively rough surfaces (Figures 1b and S5), which is due to introduction of the ultrathin MnO<sub>x</sub>/CoO<sub>x</sub> hetero-interface, confirmed by the result of energy dispersive spectroscopy (EDS) elemental mapping of BV/MnO<sub>x</sub>/CoO<sub>x</sub>

(Figure 1c), consistent with the cross-sectional SEM-EDS analysis (Figure S6). Meanwhile, the different weight percentages of BV/MnO<sub>x</sub>/CoO<sub>x</sub> can also be detected in SEM-EDS spectra (Figure S7). Finally, the excellent catalysts, i.e., FeNiOOH, were deposited onto the surface of BV/MnO<sub>x</sub>/CoO<sub>x</sub>. Specifically, the BV/MnO<sub>x</sub>/CoO<sub>x</sub>/FeNiOOH integrated system becomes rougher compared with BV/MnO<sub>x</sub>/CoO<sub>x</sub> when loading FeNiOOH because of its intrinsic structure, as confirmed by the SEM result (Figure 1d,e). In addition, the results of EDS mappings of the BV photoelectrode modified with MnO<sub>x</sub>/CoO<sub>x</sub> and FeNiOOH (BV/MnO<sub>x</sub>/CoO<sub>x</sub>/FeNiOOH) verify that the MnO<sub>x</sub>/CoO<sub>x</sub> and FeNiOOH are evenly distributed on BV (Figure S8), further proving that MnO<sub>x</sub>/CoO<sub>x</sub> and FeNiOOH were successfully modified on BV.

Of course, no obvious XRD diffraction peaks (Figure 1f) and Raman peaks (Figure 1g) corresponding to MnO<sub>x</sub>/CoO<sub>x</sub> and FeNiOOH could be detected, mainly resulting from its ultrathin thickness and lower loading capacity (Figure S9). Based on the above analysis, we can conclude that the interface regulation unit of hetero-interface has been incorporated into the interface between BV and FeNiOOH, which is essential to explore the interfacial charge transfer behavior during the PEC water splitting process.

PEC performance of the BV-based photoanode was tested via a typical three-electrode system (AM 1.5G). In Figure 2a, the pure BV photoanode exhibits a relatively low photocurrent density of 1.8 mA/cm<sup>2</sup> at 1.23 V vs. RHE, this is due to poor catalytic activity of BV towards OER and serious surface charge recombination [4,26]. When FeNiOOH is loaded onto the surface of the BV photoanode, the obtained BV/FeNiOOH photoanode shows a much higher photocurrent density of 3.5 mA/cm<sup>2</sup> at 1.23 V vs. RHE (Figure 2a) than BV, which can be attributed to the following reasons: (1) construction of the BV/FeNiOOH is a benefit for alleviating surface charge recombination by an internal electric field and (2) loading of FeNiOOH can further accelerate the OER kinetics. Nevertheless, the actual photocurrent density of the current system remains lower than the theoretical value, mainly due to the inevitable interface charge recombination [11]. To further suppress the charge recombination occurring at the BV/FeNiOOH interface, a smart interface mediator, e.g., MnO<sub>x</sub>/CoO<sub>x</sub>, was introduced into the BV/FeNiOOH system. As expected, the integrated BV/MnO<sub>x</sub>/CoO<sub>x</sub>/FeNiOOH photoanode shows a superior photocurrent density of 5.0 mA/cm<sup>2</sup> at 1.23 V vs. RHE (Figures 2a and S10), which is about three times higher than that of BV (1.8 mA/cm<sup>2</sup>). More importantly, the photocurrent density of BV/MnO<sub>x</sub>/CoO<sub>x</sub>/FeNiOOH at 1.23 V vs. RHE is greater than that of its counterparts (Figures S11 and S12), including BV/MnO<sub>x</sub>/CoO<sub>x</sub> (3.1 mA/cm<sup>2</sup>), BV/MnO<sub>x</sub>/FeNiOOH (3.8 mA/cm<sup>2</sup>), and BV/CoO<sub>x</sub>/FeNiOOH (4.1 mA/cm<sup>2</sup>), respectively, indicating the positive effect at the interfaces among the SC/TMOOH/electrolyte by introducing MnO<sub>x</sub>/CoO<sub>x</sub>.

Electrochemical impedance spectroscopy (EIS) was used to investigate the charge transfer of BV-based photoanodes under illumination. According to the Nyquist plot and fitting results ( $R_{ct}$ , CPE, and  $R_s$  represent the interface charge-transfer resistance, constant phase element, and electrolyte solution resistance, respectively), the fitted  $R_s$  values of BV, BV/FeNiOOH, and BV/MnO<sub>x</sub>/CoO<sub>x</sub>/FeNiOOH are 41.9, 44.4, and 43.4 Ω, respectively (Figure 2b and Table S1), suggesting that the above photoelectrodes have low solution resistance. For  $R_{ct}$ , the fitted  $R_{ct}$  of these samples are as follows: BV/MnO<sub>x</sub>/CoO<sub>x</sub>/FeNiOOH (389 Ω) < BV/FeNiOOH (852 Ω) < BV (991 Ω), which further reveals that the smart interface mediator can enhance the kinetics of charge transfer and boost interface charge separation, which is consistent with its higher PEC performance and surface charge separation efficiency (Figure 2c).

According to the linear sweep voltammograms (LSV) curves, the applied bias photon to current efficiencies (ABPE) of the BV/MnO<sub>x</sub>/CoO<sub>x</sub>/FeNiOOH photoanode reaches 1.5%, which is much greater than the efficiencies of BV (0.3%) and BV/FeNiOOH (1.1%, Figure 2d). In addition, the result from photoluminescence spectra (PL, Figure 2e) further indicates that BV/MnO<sub>x</sub>/CoO<sub>x</sub>/FeNiOOH exhibits lower PL intensity compared to other photoanodes, such as BV/FeNiOOH and BV. Based on the above analysis, we can conclude that the

introduction of the  $\text{MnO}_x/\text{CoO}_x$  hetero-interface into the BV/FeNiOOH system is a promising strategy for improving PEC water splitting efficiency.

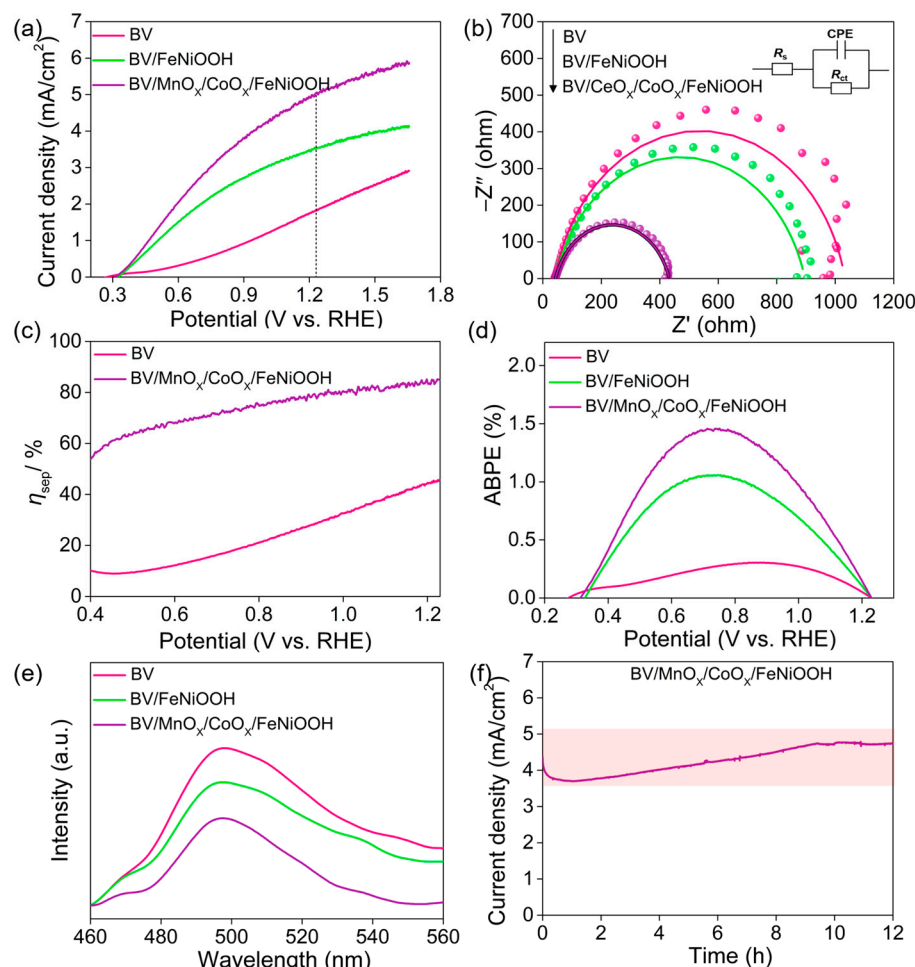


**Figure 2.** (a) LSV curves of different photoanodes measured under light irradiation; (b) EIS results under light irradiation; (c) Surface charge separation efficiencies (d) ABPE; (e) PL spectra; (f) *I-t* curve of the BV/ $\text{MnO}_x/\text{CoO}_x/\text{FeNiOOH}$  photoanode measured at 1.0 V vs. RHE.

Apart from expected PEC activity, photostability is also a vital consideration for practical applications. Herein, photostability tests were carried out for BV/ $\text{MnO}_x/\text{CoO}_x/\text{FeNiOOH}$  and BV photoanodes. As shown in Figure S13a, the photocurrent density of bare BV decreases from 1.3 to 0.98  $\text{mA}/\text{cm}^2$  under AM 1.5G illumination (7 h), which can be attributed to the  $\text{V}^{5+}$  dissolution. Interestingly, when incorporating  $\text{MnO}_x/\text{CoO}_x$  into BV/FeNiOOH, the photocurrent density of the BV/ $\text{MnO}_x/\text{CoO}_x/\text{FeNiOOH}$  photoanode is maintained for 12 h during water oxidation (Figure S13b), which is mainly due to the accelerated hole transfer behavior, and effectively inhibits the  $\text{VO}_4^{3-}$  dissolution from BV (Figure 2f).

In order to clarify the reason for the improved PEC activity due to the introduction of the  $\text{MnO}_x/\text{CoO}_x$  hetero-interface, some important characterization actions are indispensable. In general, the PEC activity is directly adjusted by the efficiencies of light harvesting, charge transfer, and surface catalytic reaction. Initially, UV-Vis diffuse reflectance spectroscopy was used to test light harvesting efficiency. As shown in Figure S14, these photoanodes, including BV/ $\text{MnO}_x/\text{CoO}_x/\text{FeNiOOH}$ , BV/FeNiOOH, and BV, show very slight changes in light absorption ability, indicating that charge separation and surface catalysis are mostly responsible for the improvement in PEC performance.

To further confirm the above assumption, intensity-modulated photocurrent spectroscopy (IMPS), developed by Peter and colleagues to explore the separation of interface charges, was performed [14,32,33]. Herein, we need to focus more on two important pa-

rameters, i.e.,  $K_{ct}$  and  $K_{rc}$ . Therefore,  $K_{ct}$  is defined as the charge transfer rate constant and  $K_{rc}$  is defined as the charge recombination rate constant. When the value of  $K_{ct}$  is higher than  $K_{rc}$ , the interface charge separation is dominant and vice versa. As shown in Figure 3a,b, for the pure BV photoanode, the  $K_{rc}$  is significantly larger than  $K_{ct}$  due to severe charge recombination. After coupling with the FeNiOOH electrocatalyst,  $K_{ct}$  is remarkably enhanced but it was still lower than the initial  $K_{rc}$  value (Figure 3b), indicating that interface charge recombination is still dominant, as supported by previous papers [11,14], consistent with the “fast” current decreasing trend observed in the  $I-t$  curve (Figure S15). More interestingly, when incorporating the hetero-interface modulation unit ( $MnO_x/CoO_x$ ) into the BV/FeNiOOH system, the  $I-t$  curve shows a slow decay trend and the value of  $K_{ct}$  is much larger than  $K_{rc}$ . This finding implies that the  $MnO_x/CoO_x$  can effectively suppress interface charge recombination via accelerating hole transfer kinetics.

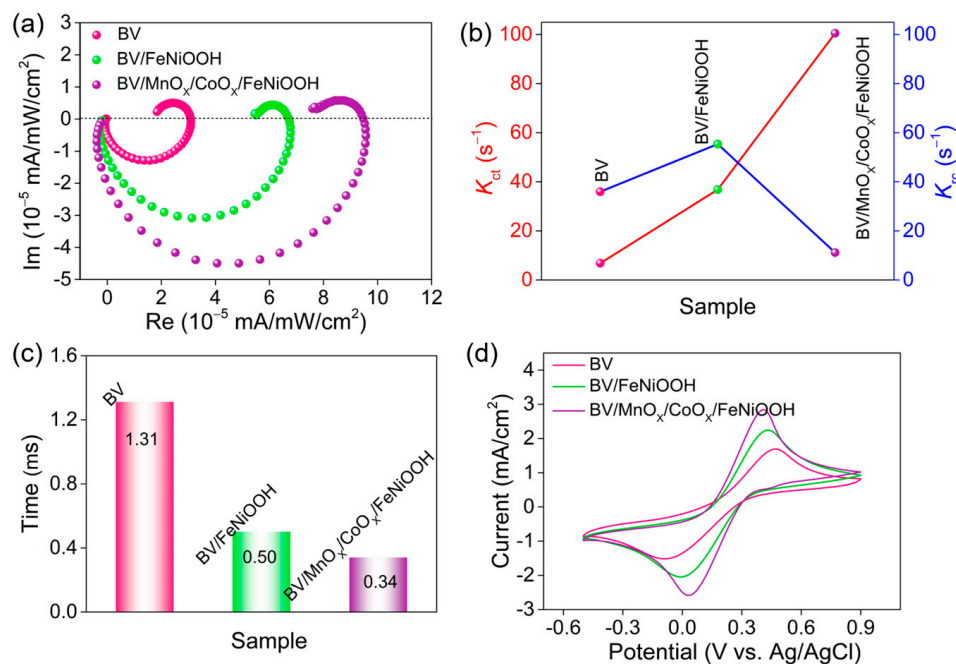


**Figure 3.** (a) IMPS responses for different samples; (b) Charge transfer rate constants and charge recombination rate constants of different photoanodes; (c) Transient time; (d) Cycle voltammetry curves measured at 50 mV/s.

In addition, based on previous work [14], the transient time ( $\tau_d$ ) of different samples can be obtained using this formula  $\tau_d = 1/(2\pi f_{max})$ , where  $f_{max}$  stands for the frequency at the lowest point. Based on this, the corresponding  $\tau_d$  values show a decreasing trend:  $BV > BV/FeNiOOH > BV/MnO_x/CoO_x/FeNiOOH$  (Figure 3c and Table S2). In particular, the  $\tau_d$  value of BV/ $MnO_x/CoO_x/FeNiOOH$  (0.34 ms) is much smaller than BV/FeNiOOH (0.50 ms), indicating the BV/ $MnO_x/CoO_x/FeNiOOH$  photoanode presents a higher charge transfer kinetics than that of BV/FeNiOOH because the hetero-interface regulation unit (e.g.,  $MnO_x/CoO_x$ ) boosts the hole transfer kinetics. Although the hetero-interface can efficiently suppress charge recombination occurring at the SC/TMOOH interface, whether these photogenerated holes are quickly transferred to the FeNiOOH surface is not known. Therefore, cyclic voltammetry (CV) was carried out to explore charge-transfer behavior by using a  $[Fe(CN)_6]^{3-}/[Fe(CN)_6]^{4-}$  probe molecule. Figure 3d demonstrates obvious characteristic redox peaks and both of anodic current and cathodic current from BV/ $MnO_x/CoO_x/FeNiOOH$  are dramatically increased compared with BV/FeNiOOH and BV photoanodes under a light condition (Figure 3d), meaning more holes have been transferred to the FeNiOOH surface via the  $MnO_x/CoO_x$  hetero-interface and participate in the OER, supported by the high charge transfer efficiency (Figure S16),  $K_{ct}$ , and  $R_{ct}$  values.

In addition to effectively suppressing interface charge recombination, it is still unknown whether the hetero-interface has a positive effect on surface catalytic activity. Accordingly, the traditional OER model, i.e., a standard three-electrode system, was carried out. BV, BV/FeNiOOH, and BV/MnO<sub>x</sub>/CoO<sub>x</sub>/FeNiOOH electrodes were tested for comparison. All the data were tested in 1 M KBi (pH 9.5) electrolyte and the potentials were converted to the reversible hydrogen electrode (RHE) reference scale via the equation:  $E_{(RHE)} = E_{(Ag/AgCl)} + (0.197 + 0.0591 \text{ pH})$  [26]. The LSV curves with *iR* compensation are shown in Figure 4a. To minimize the impact, these LSV curves are obtained under the same conditions (Figure 4a). Both BV/FeNiOOH and BV/MnO<sub>x</sub>/CoO<sub>x</sub>/FeNiOOH exhibit much better activities than pure BV film, meaning the OER catalytic activity mainly originates from the catalytic layer on BV substrate rather than the bare BV, which is also consistent with the nature of BV with low OER activity. Impressively, BV/MnO<sub>x</sub>/CoO<sub>x</sub>/FeNiOOH delivers a significantly improved activity compared with BV/FeNiOOH. The overpotentials of different samples to reach high current density are statistically compared in Figure S17. Specifically, BV/MnO<sub>x</sub>/CoO<sub>x</sub>/FeNiOOH also presents the lowest overpotentials relative to other samples (BV/FeNiOOH and BV) and only needs an overpotential of 964 mV (10 mA cm<sup>-2</sup>). These results further prove the promoting effect of the MnO<sub>x</sub>/CoO<sub>x</sub> hetero-interface on OER activity.

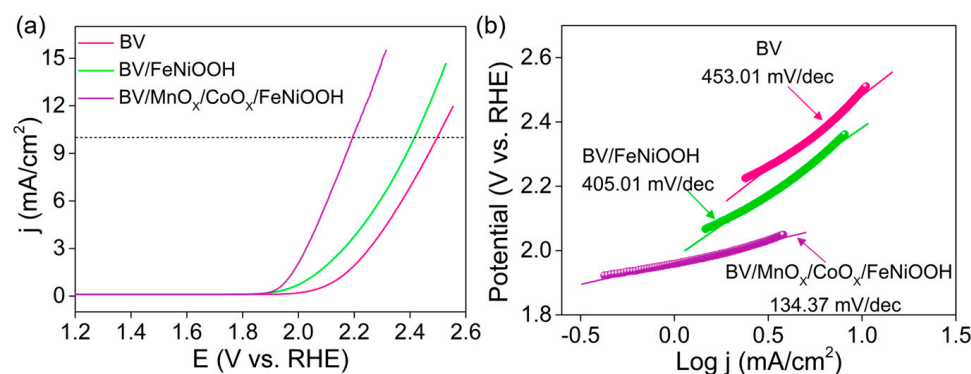


**Figure 4.** (a) *iR*-corrected LSV curves of BV/MnO<sub>x</sub>/CoO<sub>x</sub>/FeNiOOH, BV/FeNiOOH, and BV in the dark; (b) Tafel slope results of different samples.

In order to gain more insight into the positive effect of the hetero-interface on the kinetics of OER, a further measurement of the Tafel slope was performed. As presented in Figure 4b, the Tafel slope of BV/MnO<sub>x</sub>/CoO<sub>x</sub>/FeNiOOH also exhibits the lowest value of 134.37 mV dec<sup>-1</sup> than the counterparts of BV/FeNiOOH (405.01 mV dec<sup>-1</sup>) and BV (453.01 mV dec<sup>-1</sup>), revealing the superior OER kinetics of BV/MnO<sub>x</sub>/CoO<sub>x</sub>/FeNiOOH.

Apart from MnO<sub>x</sub>/CoO<sub>x</sub>, the smart hetero-interface can be successfully extended to other systems for PEC water splitting as well. Take CeO<sub>x</sub>/CoO<sub>x</sub> for example, with the introduction of the hetero-interface to the BV/FeNiOOH integrated system (Figures S18 and S19), the photocurrent density of BV/CeO<sub>x</sub>/CoO<sub>x</sub>/FeNiOOH is increased to 4.9 mA cm<sup>-2</sup> at 1.23 V<sub>RHE</sub>, which is 2.7 and 1.4 times higher than that of BV/FeNiOOH and BV photoanodes (Figure 5a,b), respectively. The improved PEC activity can be supported by ABPE (Figure 5c), EIS (Figure 5d and Table S3), and PL (Figure S20) results. Likewise, the CeO<sub>x</sub>/CoO<sub>x</sub> and FeNiOOH layer all rendered a trivial effect on light harvesting (Figure S21), indicating that the increased PEC performance can originate from efficient charge separation and surface catalysis.

To further confirm the fact that the desired charge separation comes from fast charge transfer, detailed electrochemical analyses (i.e., IMPS and CV) were conducted. From Figures 6a–c, S22 and S23, and Table S4, it is observed that, with the introduction of the hetero-interface, the  $K_{ct}$  value is much larger than  $K_{rc}$ , exhibiting the following trend: BV/CeO<sub>x</sub>/CoO<sub>x</sub>/FeNiOOH > BV/FeNiOOH > BV. Furthermore, the accelerated interface charge transfer process of BV/CeO<sub>x</sub>/CoO<sub>x</sub>/FeNiOOH is further verified by the result of CV (Figure 6d).

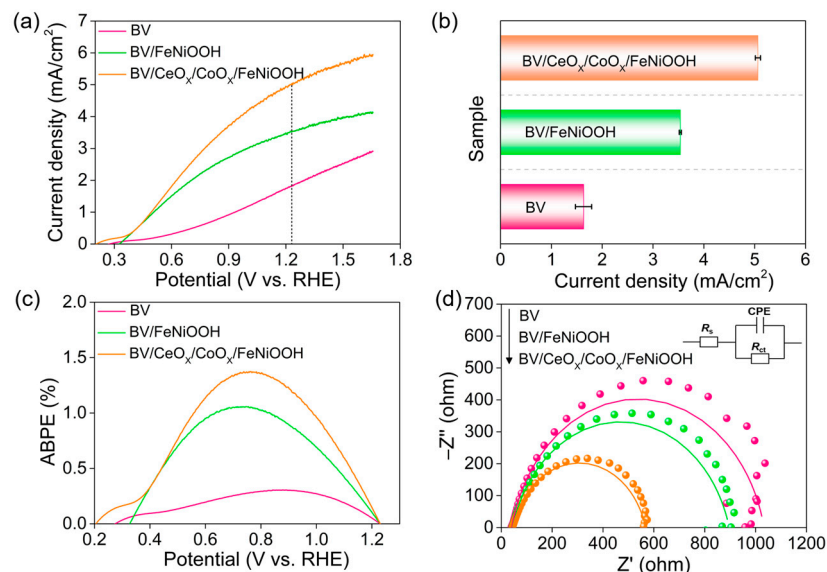


**Figure 5.** (a) LSV curves of different photoanodes under light conditions; (b) Photocurrent densities at 1.23 V<sub>RHE</sub>; (c) ABPE; (d) EIS results under light conditions.

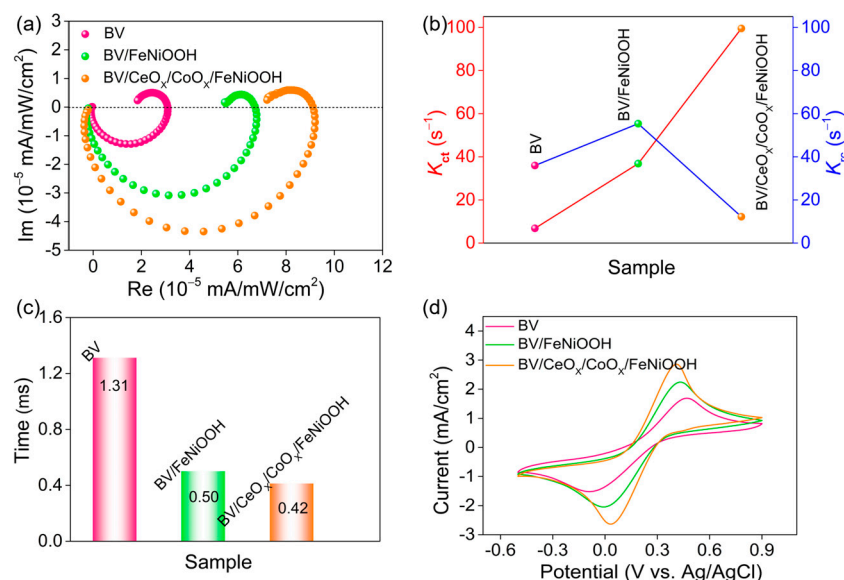


**Figure 6.** (a) IMPS responses for different samples; (b) Charge transfer rate constants and charge recombination rate constants of different photoanodes; (c) Transient time; (d) Cycle voltammetry curves of BV-based photoanodes measured at 50 mV/s.

Similarly, a typically three-electrode configuration was used to quantify the OER activity of different electrodes, including the hetero-interface mediated BV/CeO<sub>x</sub>/CoO<sub>x</sub>/FeNiOOH photoelectrode. The LSV curve (Figure 7a) reveals that BV/CeO<sub>x</sub>/CoO<sub>x</sub>/FeNiOOH exhibits lower overpotential (Figure S24) and Tafel slope (Figure 7b) compared to BV/FeNiOOH and BV, indicating that the hetero-interface can promote fast OER reaction kinetics. The above discussions fully confirm that the fast behavior of the SC/TMOOH/electrolyte can be simultaneously achieved by incorporating the hetero-interface. Such positive results may be attributed to the electron-withdrawing/donating effect from the MnO<sub>x</sub>/CoO<sub>x</sub> hetero-interface [25]. These findings provide broad universality for improving the PEC water-splitting performance in future practical applications.

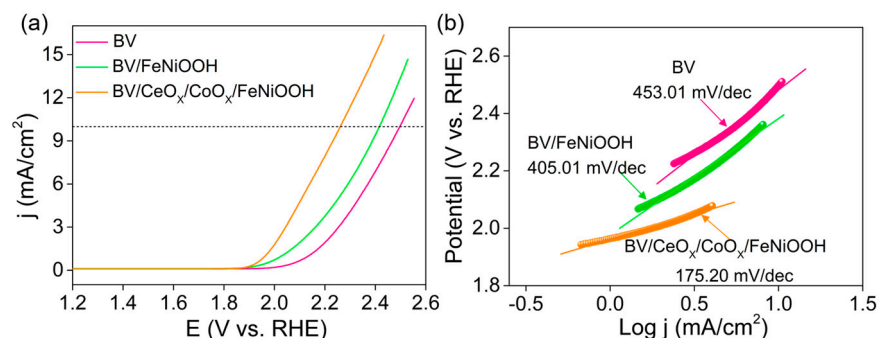


**Figure 7.** (a)  $iR$ -corrected LSV curves of BV/CeO<sub>x</sub>/CoO<sub>x</sub>/FeNiOOH, BV/FeNiOOH, and BV in the dark; (b) Tafel slope of relevant samples.

#### 4. Conclusions

In this work, a hetero-interface regulated SC/TMOOH coupled system for PEC water splitting was successfully constructed and the optimized BV/MnO<sub>x</sub>/CoO<sub>x</sub>/FeNiOOH photoanode shows a high photocurrent density of 5.0 mA/cm<sup>2</sup> at 1.23 V vs. RHE under 1 sun AM 1.5G illumination, along with good stability. Detailed electrochemical characterization techniques, such as IMPS, OER, and CV, confirm that the expected PEC performance is attributed to the accelerated kinetic behavior at the interfaces among SC/TMOOH/electrolyte by introducing MnO<sub>x</sub>/CoO<sub>x</sub> simultaneously. Typically, BV/MnO<sub>x</sub>/CoO<sub>x</sub>/FeNiOOH shows the highest hole transfer kinetic (100.5 s<sup>-1</sup>), which is 14.8 times higher than that of pure BV (6.8 s<sup>-1</sup>). In addition, under dark conditions, the Tafel slope of BV/MnO<sub>x</sub>/CoO<sub>x</sub>/FeNiOOH is decreased from 453.01 to 134.37 mV dec<sup>-1</sup>. More importantly, the hetero-interface can be successfully extended to CeO<sub>x</sub>/CoO<sub>x</sub> and exhibit high PEC performance. It is widely believed that our hetero-interface engineering provides an effective strategy for PEC water splitting and energy conversion field.

**Supplementary Materials:** The following supporting information can be downloaded at: <https://www.mdpi.com/article/10.3390/separations11040109/s1>, Figure S1: SEM images of the BV; Figure S2: XRD of FTO and BV; Figure S3: XPS spectra of BV; Figure S4: Raman spectra of BV; Figure S5: SEM image of BV/MnO<sub>x</sub>/CoO<sub>x</sub>; Figure S6: Cross-sectional SEM-Energy disperse spectroscopy (EDS) analysis of the BV/MnO<sub>x</sub>/CoO<sub>x</sub>; Figure S7: SEM-EDS spectra of BV/MnO<sub>x</sub>/CoO<sub>x</sub>; Figure S8: SEM-EDS elemental mapping images of BV/MnO<sub>x</sub>/CoO<sub>x</sub>/FeNiOOH; Figure S9: (a) XRD of BV and BV/MnO<sub>x</sub>/CoO<sub>x</sub>. (b) Raman spectra of BV/MnO<sub>x</sub>/CoO<sub>x</sub>; Figure S10: Photocurrent densities of BV/MnO<sub>x</sub>/CoO<sub>x</sub>/FeNiOOH, BV/FeNiOOH, and BV photoanodes; Figure S11: LSV curves of different photoanodes; Figure S12: LSV curves of different photoanodes; Figure S13: (a)  $I-t$  curve of the BV photoanode. (b) The picture of oxygen evolution; Figure S14: UV/Vis diffuse reflectance spectra of different samples; Figure S15:  $I-t$  curves of different photoanodes; Figure S16: Charge transfer efficiencies for different samples; Figure S17: The overpotentials of different samples at 10 mA/cm<sup>2</sup>; Figure S18: SEM image of (a) BV/CeO<sub>x</sub>/CoO<sub>x</sub> and (b) BV/CeO<sub>x</sub>/CoO<sub>x</sub>/FeNiOOH; Figure S19: (a) XRD of FTO, BV, BV/FeNiOOH, and BV/CeO<sub>x</sub>/CoO<sub>x</sub>/FeNiOOH. (b) Raman spectra of different samples; Figure S20: PL spectra of different photoanodes with excitation of 355 nm wavelength; Figure S21: UV/Vis diffuse reflectance spectroscopy of different samples; Figure S22:  $I-t$  curves of different photoanodes; Figure S23: Charge transfer efficiencies; Figure S24: The overpotentials of different samples; Table S1: EIS of different samples; Table S2: Transit time values of different samples; Table S3: EIS of different samples; Table S4: Transit time values of different samples.

**Author Contributions:** L.X. (Li Xu 1) and X.N. conceived and designed experiments. L.X. (Li Xu 1), J.Q., L.X. (Li Xu 2), Q.W., P.C., X.C. and Z.A. directed the experiments and revised the paper. (Li Xu 1) performed the measurements. M.L., (Li Xu 2), C.L. and S.M. accomplished XPS, XRD, and PEC measurements and consulted the literature. (Li Xu 2), J.Q. and X.N. wrote the paper. All authors reviewed the paper. All authors have read and agreed to the published version of the manuscript.

**Funding:** National Natural Science Foundation of China (22202126, 52273186, 51873100 and 62105194), San qin scholars innovation teams in Shaanxi Province, China, International Joint Research Center of Shaanxi Province for Photoelectric Materials Science, and International Science and Technology Cooperation Project of Shaanxi Province, China (2021KW-20).

**Data Availability Statement:** The data presented in this study are available within the article and its Supplementary Materials.

**Acknowledgments:** The authors are thankful to the National Natural Science Foundation of China, San Qin Scholars innovation teams in Shaanxi Province, China, International Joint Research Center of Shaanxi Province for Photoelectric Materials Science, and International Science and Technology Cooperation Project of Shaanxi Province, China (2021KW-20).

**Conflicts of Interest:** The authors declare no conflicts of interest.

## References

1. Holmes-Gentle, I.; Tembhurne, S.; Suter, C.; Haussener, S. Kilowatt-scale solar hydrogen production system using a concentrated integrated photoelectrochemical device. *Nat. Energy* **2023**, *8*, 586–596. [\[CrossRef\]](#)
2. Liu, C.; Zhang, N.; Li, Y.; Fan, R.; Wang, W.; Feng, J.; Liu, C.; Wang, J.; Hao, W.; Li, Z.; et al. Long-term durability of metastable  $\beta$ -Fe<sub>2</sub>O<sub>3</sub> photoanodes in highly corrosive seawater. *Nat. Commun.* **2023**, *14*, 4266. [\[CrossRef\]](#)
3. Xiao, Y.; Kong, X.; Vanka, S.; Dong, W.J.; Zeng, G.; Ye, Z.; Sun, K.; Navid, I.A.; Zhou, B.; Toma, F.M.; et al. Oxynitrides enabled photoelectrochemical water splitting with over 3,000 hrs stable operation in practical two-electrode configuration. *Nat. Commun.* **2023**, *14*, 2047. [\[CrossRef\]](#)
4. Hilbrands, A.M.; Zhang, S.; Zhou, C.; Melani, G.; Wi, D.H.; Lee, D.; Xi, Z.; Head, A.R.; Liu, M.; Galli, G.; et al. Impact of Varying the Photoanode/Catalyst Interfacial Composition on Solar Water Oxidation: The Case of BiVO<sub>4</sub>(010)/FeOOH Photoanodes. *J. Am. Chem. Soc.* **2023**, *145*, 23639–23650. [\[CrossRef\]](#)
5. Corby, S.; Rao, R.R.; Steier, L.; Durrant, J.R. The kinetics of metal oxide photoanodes from charge generation to catalysis. *Nat. Rev. Mater.* **2021**, *6*, 1136–1155. [\[CrossRef\]](#)
6. Zhang, K.; Jin, B.; Park, C.; Cho, Y.; Song, X.; Shi, X.; Zhang, S.; Kim, W.; Zeng, H.; Park, J.H. Black phosphorene as a hole extraction layer boosting solar water splitting of oxygen evolution catalysts. *Nat. Commun.* **2019**, *10*, 2001. [\[CrossRef\]](#)
7. Zhang, B.; Yu, S.; Dai, Y.; Huang, X.; Chou, L.; Lu, G.; Dong, G.; Bi, Y. Nitrogen-incorporation activates NiFeO<sub>x</sub> catalysts for efficiently boosting oxygen evolution activity and stability of BiVO<sub>4</sub> photoanodes. *Nat. Commun.* **2021**, *12*, 6969. [\[CrossRef\]](#)
8. Kim, T.W.; Choi, K.-S. Nanoporous BiVO<sub>4</sub> Photoanodes with Dual-Layer Oxygen Evolution Catalysts for Solar Water Splitting. *Science* **2014**, *343*, 990–994. [\[CrossRef\]](#)
9. Wu, Z.; Liu, X.; Li, H.; Sun, Z.; Cao, M.; Li, Z.; Fang, C.; Zhou, J.; Cao, C.; Dong, J.; et al. A semiconductor-electrocatalyst nano interface constructed for successive photoelectrochemical water oxidation. *Nat. Commun.* **2023**, *14*, 2574. [\[CrossRef\]](#)
10. Liu, W.; Liu, H.; Dang, L.; Zhang, H.; Wu, X.; Yang, B.; Li, Z.; Zhang, X.; Lei, L.; Jin, S. Amorphous Cobalt–Iron Hydroxide Nanosheet Electrocatalyst for Efficient Electrochemical and Photo-Electrochemical Oxygen Evolution. *Adv. Funct. Mater.* **2017**, *27*, 1603904. [\[CrossRef\]](#)
11. Ning, X.; Du, P.; Han, Z.; Chen, J.; Lu, X. Insight into the Transition-Metal Hydroxide Cover Layer for Enhancing Photoelectrochemical Water Oxidation. *Angew. Chem. Int. Ed.* **2021**, *60*, 3504–3509. [\[CrossRef\]](#)
12. Zhang, B.; Huang, X.; Zhang, Y.; Lu, G.; Chou, L.; Bi, Y. Unveiling the Activity and Stability Origin of BiVO<sub>4</sub> Photoanodes with FeNi Oxyhydroxides for Oxygen Evolution. *Angew. Chem. Int. Ed.* **2020**, *59*, 18990–18995. [\[CrossRef\]](#)
13. Zhang, Y.; Xu, L.; Liu, B.; Wang, X.; Wang, T.; Xiao, X.; Wang, S.; Huang, W. Engineering BiVO<sub>4</sub> and Oxygen Evolution Cocatalyst Interfaces with Rapid Hole Extraction for Photoelectrochemical Water Splitting. *ACS Catal.* **2023**, *13*, 5938–5948. [\[CrossRef\]](#)
14. Ning, X.; Lu, B.; Zhang, Z.; Du, P.; Ren, H.; Shan, D.; Chen, J.; Gao, Y.; Lu, X. An Efficient Strategy for Boosting Photogenerated Charge Separation by Using Porphyrins as Interfacial Charge Mediators. *Angew. Chem. Int. Ed.* **2019**, *58*, 16800–16805. [\[CrossRef\]](#)
15. Chen, R.; Meng, L.; Xu, W.; Li, L. Cocatalysts-Photoanode Interface in Photoelectrochemical Water Splitting: Understanding and Insights. *Small* **2024**, *20*, 2304807. [\[CrossRef\]](#)
16. Ma, Y.; Kafizas, A.; Pendlebury, S.R.; Le Formal, F.; Durrant, J.R. Photoinduced Absorption Spectroscopy of CoPi on BiVO<sub>4</sub>: The Function of CoPi during Water Oxidation. *Adv. Funct. Mater.* **2016**, *26*, 4951–4960. [\[CrossRef\]](#)
17. Zhang, X.; Zhai, P.; Zhang, Y.; Wu, Y.; Wang, C.; Ran, L.; Gao, J.; Li, Z.; Zhang, B.; Fan, Z.; et al. Engineering Single-Atomic Ni-N<sub>4</sub>-O Sites on Semiconductor Photoanodes for High-Performance Photoelectrochemical Water Splitting. *J. Am. Chem. Soc.* **2021**, *143*, 20657–20669. [\[CrossRef\]](#)
18. Song, Y.; Zhang, X.; Zhang, Y.; Zhai, P.; Li, Z.; Jin, D.; Cao, J.; Wang, C.; Zhang, B.; Gao, J. Engineering MoO<sub>x</sub>/MXene Hole Transfer Layers for Unexpected Boosting of Photoelectrochemical Water Oxidation. *Angew. Chem.* **2022**, *134*, e202200946. [\[CrossRef\]](#)
19. Ren, H.; Dittrich, T.; Ma, H.; Hart, J.N.; Fengler, S.; Chen, S.; Li, Y.; Wang, Y.; Cao, F.; Schieda, M.; et al. Manipulation of Charge Transport by Metallic V<sub>13</sub>O<sub>16</sub> Decorated on Bismuth Vanadate Photoelectrochemical Catalyst. *Adv. Mater.* **2019**, *31*, 1807204. [\[CrossRef\]](#)
20. Yin, H.; Li, D.; Wang, X.; Li, C. Surface Passivation Effect of Ferrihydrite with Hole-Storage Ability in Water Oxidation on BiVO<sub>4</sub> Photoanode. *J. Phys. Chem. C* **2021**, *125*, 8369–8375. [\[CrossRef\]](#)

21. Zhang, Z.; Huang, X.; Zhang, B.; Bi, Y. High-performance and stable BiVO<sub>4</sub> photoanodes for solar water splitting via phosphorus-oxygen bonded FeNi catalysts. *Energy Environ. Sci.* **2022**, *15*, 2867–2873. [[CrossRef](#)]
22. Yang, N.; Zhang, S.; Xiao, Y.; Qi, Y.; Bao, Y.; Xu, P.; Jin, S.; Zhang, F. Insight into the Key Restriction of BiVO<sub>4</sub> Photoanodes Prepared by Pyrolysis Method for Scalable Preparation. *Angew. Chem. Int. Ed.* **2023**, *62*, e202308729. [[CrossRef](#)]
23. Ning, X.; Yin, D.; Fan, Y.; Zhang, Q.; Du, P.; Zhang, D.; Chen, J.; Lu, X. Plasmon-Enhanced Charge Separation and Surface Reactions Based on Ag-Loaded Transition-Metal Hydroxide for Photoelectrochemical Water Oxidation. *Adv. Energy Mater.* **2021**, *11*, 2100405. [[CrossRef](#)]
24. Zhong, M.; Hisatomi, T.; Kuang, Y.; Zhao, J.; Liu, M.; Iwase, A.; Jia, Q.; Nishiyama, H.; Minegishi, T.; Nakabayashi, M.; et al. Surface Modification of CoO<sub>x</sub> Loaded BiVO<sub>4</sub> Photoanodes with Ultrathin p-Type NiO Layers for Improved Solar Water Oxidation. *J. Am. Chem. Soc.* **2015**, *137*, 5053–5060. [[CrossRef](#)]
25. Yang, G.; Li, Y.; Pang, H.; Chang, K.; Ye, J. Ultrathin Cobalt–Manganese Nanosheets: An Efficient Platform for Enhanced Photoelectrochemical Water Oxidation with Electron-Donating Effect. *Adv. Funct. Mater.* **2019**, *29*, 1904622. [[CrossRef](#)]
26. Liu, B.; Wang, X.; Zhang, Y.; Xu, L.; Wang, T.; Xiao, X.; Wang, S.; Wang, L.; Huang, W. A BiVO<sub>4</sub> Photoanode with a VO<sub>x</sub> Layer Bearing Oxygen Vacancies Offers Improved Charge Transfer and Oxygen Evolution Kinetics in Photoelectrochemical Water Splitting. *Angew. Chem. Int. Ed.* **2023**, *62*, e202217346. [[CrossRef](#)]
27. Zhang, B.; Wang, L.; Zhang, Y.; Ding, Y.; Bi, Y. Ultrathin FeOOH nanolayers with abundant oxygen vacancies on BiVO<sub>4</sub> photoanodes for efficient water oxidation. *Angew. Chem. Int. Ed.* **2018**, *57*, 2248–2252. [[CrossRef](#)]
28. Song, Y.; Ren, Y.; Cheng, H.; Jiao, Y.; Shi, S.; Gao, L.; Xie, H.; Gao, J.; Sun, L.; Hou, J. Metal-Organic Framework Glass Catalysts from Melting Glass-Forming Cobalt-Based Zeolitic Imidazolate Framework for Boosting Photoelectrochemical Water Oxidation. *Angew. Chem. Int. Ed.* **2023**, *62*, e202306420. [[CrossRef](#)]
29. Wang, J.; Zuo, L.; Guo, Z.; Yang, C.; Jiang, Y.; Huang, X.; Wu, L.; Tang, Z. Al<sub>2</sub>O<sub>3</sub>-coated BiVO<sub>4</sub> Photoanodes for Photoelectrocatalytic Regioselective C–H Activation of Aromatic Amines. *Angew. Chem. Int. Ed.* **2023**, *135*, e202315478. [[CrossRef](#)]
30. Zhang, R.; Ning, X.; Wang, Z.; Zhao, H.; He, Y.; Han, Z.; Du, P.; Lu, X. Significantly Promoting the Photogenerated Charge Separation by Introducing an Oxygen Vacancy Regulation Strategy on the FeNiOOH Co-Catalyst. *Small* **2022**, *18*, 2107938. [[CrossRef](#)]
31. Wu, H.; Zhang, L.; Du, A.; Irani, R.; van de Krol, R.; Abdi, F.F.; Ng, Y.H. Low-bias photoelectrochemical water splitting via mediating trap states and small polaron hopping. *Nat. Commun.* **2022**, *13*, 6231. [[CrossRef](#)]
32. Li, F.; Yang, H.; Zhuo, Q.; Zhou, D.; Wu, X.; Zhang, P.; Yao, Z.; Sun, L. A Cobalt@Cucurbit[5]uril Complex as a Highly Efficient Supramolecular Catalyst for Electrochemical and Photoelectrochemical Water Splitting. *Angew. Chem. Int. Ed.* **2021**, *60*, 1976–1985. [[CrossRef](#)]
33. Yu, F.; Li, F.; Yao, T.; Du, J.; Liang, Y.; Wang, Y.; Han, H.; Sun, L. Fabrication and Kinetic Study of a Ferrihydrite-Modified BiVO<sub>4</sub> Photoanode. *ACS Catal.* **2017**, *7*, 1868–1874. [[CrossRef](#)]

**Disclaimer/Publisher’s Note:** The statements, opinions and data contained in all publications are solely those of the individual author(s) and contributor(s) and not of MDPI and/or the editor(s). MDPI and/or the editor(s) disclaim responsibility for any injury to people or property resulting from any ideas, methods, instructions or products referred to in the content.